nature astronomy

Article

https://doi.org/10.1038/s41550-024-02249-0

Identification of the weak-to-strong transition in Alfvénic turbulence from space plasma

Received: 17 January 2023

Accepted: 11 March 2024

Published online: 12 April 2024

Check for updates

Siqi Zhao[1,5], Huirong Yan[1,5] ✉, Terry Z. Liu[2] ✉, Ka Ho Yuen[3] & Huizi Wang[4]

Plasma turbulence is a ubiquitous dynamical process that transfers energy across many spatial and temporal scales in astrophysical and space plasma systems. Although the theory of anisotropic magnetohydrodynamic (MHD) turbulence has successfully described natural phenomena, its core prediction of an Alfvénic transition from weak to strong MHD turbulence when energy cascades from large to small scales has not been observationally confirmed. Here we report evidence for the Alfvénic weak-to-strong transition in small-amplitude, turbulent MHD fluctuations in Earth's magnetosheath using data from four Cluster spacecraft. Our observations demonstrate the universal existence of strong turbulence accompanied by weak turbulent fluctuations on large scales. Moreover, we find that the nonlinear interactions of MHD turbulence are crucial to the energy cascade, as they broaden the cascade directions and fluctuating frequencies. The observed connection between weak and strong MHD turbulence systems may be present in many astrophysical environments, such as star formation, energetic particle transport, turbulent dynamos, and solar corona or solar wind heating.

The theory of anisotropic magnetohydrodynamic (MHD) turbulence has been widely accepted and adopted for plasma systems ranging from clusters of galaxies, the interstellar medium and accretion disks to the heliosphere[1–3]. One of the most crucial predictions of the theory is an Alfvénic transition from weak to strong MHD turbulence when energy cascades from large to small scales[4,5]. The self-organized process from weak to strong MHD turbulence is the cornerstone of understanding the energy cascade in the complete picture of MHD turbulence.

The critical balance model is attractive for describing the physical behaviour of incompressible MHD turbulence[4]. When $\tau_A \ll \tau_{nl}$ (referred to as weak MHD turbulence), weak interactions among the counter-propagating wave packets transfer energy to higher $k_\perp$ whereas no energy cascades to higher $k_\parallel$, where $\tau_A = 1/(k_\parallel V_A)$ is the linear Alfvén wave time, $\tau_{nl} = 1/(k_\perp \delta V_\perp)$ is the nonlinear time, V_A is the Alfvén speed, $\delta V_\perp$ is the fluctuating velocity perpendicular to the background magnetic field ($\mathbf{B}_0$), and $k_\perp$ and $k_\parallel$ are wavenumbers perpendicular and parallel to $\mathbf{B}_0$ (ref. 6). As turbulence cascades to smaller scales, nonlinearity strengthens until it reaches the critical balance ($\tau_A \approx \tau_{nl}$) at the transition scale (λ_{CB}). On scales smaller than λ_{CB}, Alfvén wave packets are statistically destroyed in one τ_A. In addition to the first-order interactions of counter-propagating waves, all higher orders of interactions can contribute to create strong MHD turbulence[4,7]. In compressible MHD, small-amplitude fluctuations can be decomposed into three eigenmodes (namely, Alfvén, fast and slow modes) in a homogeneous plasma[8–12]. Alfvén modes decoupled from compressible MHD turbulence, which are linearly independent of fast and slow modes, show similar properties to those in incompressible MHD turbulence, for example, the Kolmogorov spectrum and the

[1]Institut für Physik und Astronomie, Universität Potsdam, Potsdam, Germany. [2]Department of Earth, Planetary, and Space Sciences, University of California, Los Angeles, Los Angeles, CA, USA. [3]Theoretical Division, Los Alamos National Laboratory, Los Alamos, NM, USA. [4]Shandong Key Laboratory of Optical Astronomy and Solar-Terrestrial Environment, Institute of Space Sciences, Shandong University, Weihai, People's Republic of China. [5]Present address: Deutsches Elektronen-Synchrotron DESY, Zeuthen, Germany. ✉e-mail: huirong.yan@desy.de; terryliuzixu@ucla.edu

https://doi.org/10.1038/s41550-024-02249-0

scale-dependent anisotropy[8,13]. Additionally, numerical simulations have confirmed that the Alfvénic weak-to-strong transition occurs in both incompressible MHD turbulence and Alfvén modes decomposed from compressible MHD turbulence[9,14,15].

However, this transition has not been confirmed from observations. In this study, we present evidence for the Alfvénic weak-to-strong transition and estimate the transition scale λ_{CB} in Earth's magnetosheath using data from the four Cluster spacecraft[16]. Earth's magnetosheath offers a representative environment for studying plasma turbulence, given that most astrophysical and space plasmas with finite plasma β are compressible, where β is the ratio of the plasma to magnetic pressure.

Results

Here we present an overview of fluctuations observed by Cluster-1 in geocentric-solar-ecliptic (GSE) coordinates during 23:00–10:00 Universal Time (UT) on 2–3 December in Fig. 1. During this period, the four Cluster spacecraft flew in a tetrahedral formation with relative separation $d_{sc} \approx 200$ km (around three proton inertial lengths $d_i \approx 74$ km) on the flank of Earth's magnetosheath around [1.2, 18.2, −5.7] R_E (Earth radius). We chose this time interval to study the Alfvénic weak-to-strong transition because the fluctuations satisfy the following criteria. First, the background magnetic field ($\mathbf{B}$) measured by the fluxgate magnetometer[17] and the proton bulk velocity ($\mathbf{V}_p$) measured by the Cluster Ion Spectrometer (CIS)[18] were relatively stable, as shown in Fig. 1a,b. Second, we cross-verified the reliability of the plasma data based on the consistency between the proton density (N_p) measured by CIS and the electron density (N_e) measured by the Waves of High frequency and Sounder for Probing of Electron density by Relaxation (WHISPER)[19], as shown in Fig. 1c.

We set a moving time window with a length of 5 h and a moving step of 5 min. The selection of a 5 h length ensured that we obtained measurements at low frequencies (large scales) while the mean magnetic field ($\mathbf{B}_0$) within the moving time window was approaching the local mean field at the selected largest spatial scale. The uniformity of $\mathbf{B}_0$ was independent of the transformation between real and wavevector space; however, it differed from the theoretically expected local mean field at each scale. To assess such differences, Supplementary Fig. 1 shows that the local mean field at different scales is closely aligned with $\mathbf{B}_0$ most of the time, suggesting that using $\mathbf{B}_0$ to approximate the local mean field is acceptable. To further address this limitation of the mode decomposition method, which relies on a perturbative treatment of fluctuations in the presence of a uniform background magnetic field[8], we provide results obtained using various time window lengths, all of which show similar conclusions (Supplementary Fig. 2).

Third, Fig. 1d shows the spectral slopes of the trace magnetic field and proton velocity power calculated by a fast Fourier transform with three-point centred smoothing in each time window. These spectral slopes at the spacecraft-frame frequency $f_{sc} \approx [0.001\,\text{Hz}, 0.1f_{ci}]$ are close to −5/3 or −3/2 (the proton gyro-frequency $f_{ci} \approx 0.24$ Hz), suggesting that the turbulent fluctuations were in a fully developed state. The remaining magnetosheath fluctuations with spectra close to f_{sc}^{-1} are typically populated by uncorrelated fluctuations[20,21] and are beyond the scope of the present paper. Figure 1e shows that the average proton plasma β_p was around 1.4. Finally, Fig. 1f shows that the turbulent Alfvén number $M_{A,turb} \equiv \delta V_p/V_A \approx \delta B/(2B_0) \approx 0.33$, suggesting that the fluctuations include substantial Alfvénic components and satisfy the small-amplitude fluctuation assumption (the nonlinear terms δV_p^2 and δB^2 are weaker than the linear terms $V_A \delta V_p$ and $B_0 \delta B$). Nevertheless, the average magnetic compressibility $C_\parallel(f_{sc}) = \frac{|\delta B_\parallel(f_{sc})|^2}{|\delta B_\parallel(f_{sc})|^2 + |\delta B_\perp(f_{sc})|^2} \approx 0.34$, indicating that the fluctuations are a mixture of Alfvén and compressible magnetosonic modes (fast and slow)[22], where $\delta B_\parallel$ and $\delta B_\perp$ are the fluctuating magnetic fields parallel and perpendicular to $\mathbf{B}_0$.

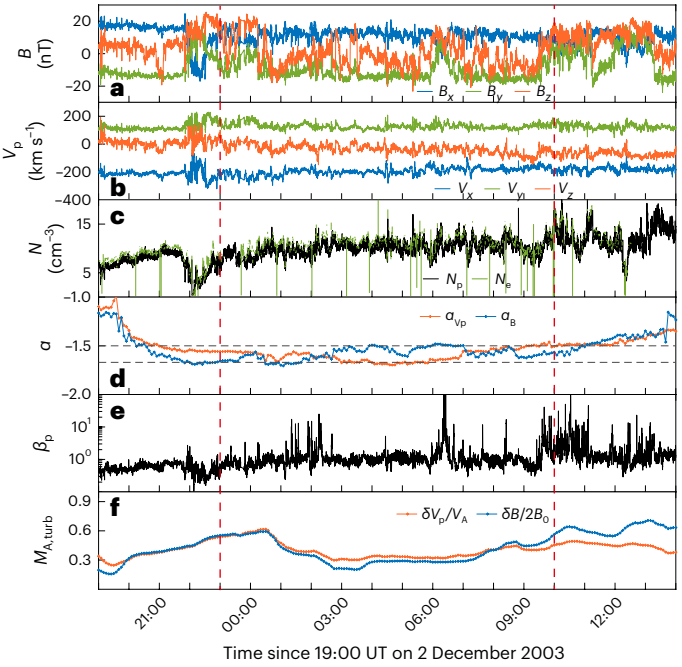

Fig. 1 | Overview of fluctuations measured by Cluster-1 in Earth's magnetosheath on 2–3 December 2003. a–f, Data are displayed in GSE coordinates. **a**, Magnetic field components (B_X, B_Y and B_Z). **b**, Proton bulk velocity (V_X, V_Y and V_Z). **c**, Proton and electron densities. **d**, Spectral slopes (α) of magnetic field and proton velocity fluctuations between 0.001 Hz and $0.1f_{ci}$. The two horizontal lines represent $\alpha = -5/3$ and $-3/2$. **e**, Proton plasma β_p. **f**, Turbulent Alfvén Mach number ($M_{A,turb} = \delta V_p/V_A$) and half of the relative amplitudes of the magnetic field ($\delta B/(2B_0)$), where δV_p and δB are the root mean square of the proton velocity and magnetic field fluctuations, respectively. The fluctuations analysed in detail were observed during 23:00–10:00 UT on 2–3 December and are marked between the two vertical dashed lines.

Due to the homogeneous and stationary state of the turbulence (Supplementary Fig. 3), we can utilize frequency–wavenumber distributions of Alfvénic power, that is magnetic power $P_{B_A}(k_\perp, k_\parallel, f_{sc})$ and proton velocity power $P_{V_A}(k_\perp, k_\parallel, f_{sc})$, to investigate the structure of the turbulence. Alfvénic fluctuations were extracted in each time window based on their incompressibility and fluctuating directions perpendicular to $\mathbf{B}_0$ (Methods). To distinguish between spatial evolution and temporal evolution without relying on any spatio-temporal hypothesis, we determined the wavevectors by combining the singular value decomposition method[23] (to obtain $\hat{\mathbf{k}}_{SVD}$) and a multispacecraft timing analysis[24] (to obtain $\hat{\mathbf{k}}_A$). Note that $\hat{\mathbf{k}}_A$ was not completely aligned with $\hat{\mathbf{k}}_{SVD}$. Namely, $\hat{\mathbf{k}}_A$ could deviate from $\hat{\mathbf{k}}_{SVD}$ by angle η (Supplementary Fig. 4). Thus, we present results for $\eta < 10°$, $\eta < 15°$, $\eta < 20°$, $\eta < 25°$ and $\eta < 30°$. Given the marginal impact of different choices of η (Supplementary Figs. 5 and 6), the spectral results are displayed by taking the dataset for $\eta < 30°$ as an example without loss of generality. The fluctuations, in this event, count for 42% of the total Alfvénic fluctuations.

To ensure the reliability of the wavenumber determination, we established minimum thresholds $k > 1/(100d_{sc})$ and $k_\parallel > 10^{-5}$ km^{-1}. Consequently, our observations exclude the ideal two-dimensional (2D) case ($k_\parallel = 0$). Here, τ_A is infinity, indicating persistent strong nonlinearity[25,26]. Nevertheless, quasi-2D (small $k_\parallel$) modes are present, as $k_\parallel$ is much smaller than $k_\perp$ at small wavenumbers (Fig. 2). These quasi-2D fluctuations satisfy $\tau_A < \tau_{nl}$, as shown in Fig. 3c, and exhibit weak nonlinearity. This weak turbulent state occurs since $\delta B_A^2(k_\perp, k_\parallel)/B_0^2$ is very low, where the Alfvénic magnetic energy density at $k_\perp$ and $k_\parallel$ is calculated with $\delta B_A^2(k_\perp, k_\parallel) = \sum_{k_\perp=k_\perp}^{k_\perp\to\infty} \sum_{k_\parallel=k_\parallel}^{k_\parallel\to\infty} \int_0^\infty P_{B_A}(k_\perp, k_\parallel, f_{sc})\, \mathrm{d}f_{sc}$.

https://doi.org/10.1038/s41550-024-02249-0

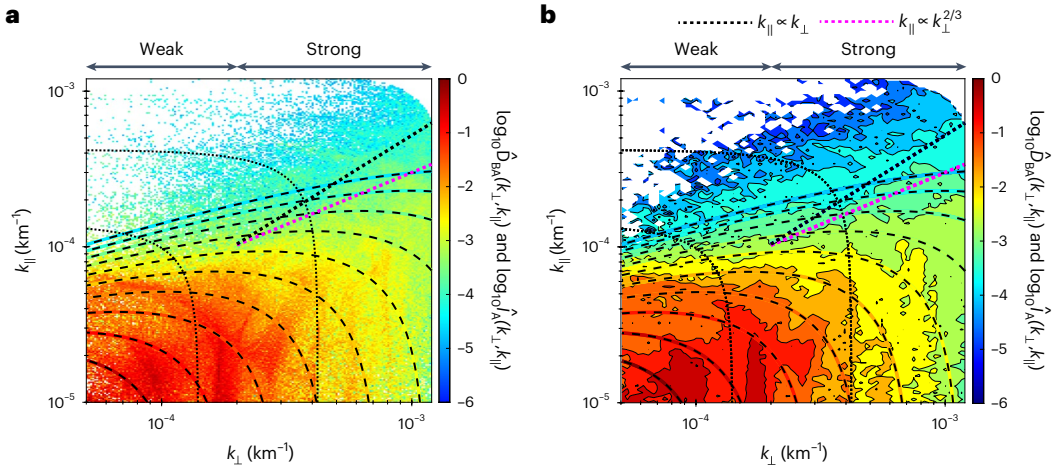

Fig. 2 | Comparison between wavenumber distributions of Alfvénic magnetic energy $\hat{D}_{B_A}(k_\perp, k_\parallel)$ and the theoretical energy spectra $\hat{I}_A(k_\perp, k_\parallel)$. **a**, 2D spectral image of $\hat{D}_{B_A}(k_\perp, k_\parallel)$ with a high resolution (400 × 400 bins). **b**, 2D filled contours of $\hat{D}_{B_A}(k_\perp, k_\parallel)$ with low-resolution binning (150 × 150 bins), to clarify the contours. In each panel, $\hat{I}_A(k_\perp, k_\parallel)$ at $L_0 \approx 4.6 \times 10^4$ km is displayed by colour contours with black dashed curves with the same colour map as $\hat{D}_{B_A}(k_\perp, k_\parallel)$. The black dotted curves mark $k = \sqrt{k_\parallel^2 + k_\perp^2} = 0.01/d_i$ and $0.03/d_i$. These figures utilize the dataset for $\eta < 30°$.

Evidence for the Alfvénic weak-to-strong transition

The 2D wavenumber distributions of magnetic energy are calculated by

$$D_{B_A}(k_\perp, k_\parallel) = \int_0^\infty P_{B_A}(k_\perp, k_\parallel, f_{sc})\, \mathrm{d}\, f_{sc}. \quad (1)$$

$\hat{D}_{B_A}(k_\perp, k_\parallel) = D_{B_A}(k_\perp, k_\parallel)/D_{B_A,\max}$ is normalized by the maximum magnetic energy in all $(k_\perp, k_\parallel)$ bins, as displayed by the spectral image and contours in Fig. 2. Compared to the isotropic dotted curves, $\hat{D}_{B_A}(k_\perp, k_\parallel)$ is prominently distributed along the $k_\perp$ direction, suggesting a faster perpendicular cascade. This anisotropic behaviour is more pronounced at higher wavenumbers, consistent with previous simulations and observations[9,13,27,28].

Moreover, $\hat{D}_{B_A}(k_\perp, k_\parallel)$ is compared with the modelled 2D theoretical energy spectra based on strong turbulence[4,29]:

$$I_A(k_\perp, k_\parallel) \propto k_\perp^{-7/3} \exp\left(-\frac{L_0^{1/3}|k_\parallel|}{M_{A,\mathrm{turb}}^{4/3} k_\perp^{2/3}}\right), \quad (2)$$

where the injection scale $L_0 \approx [4.6 \times 10^4, 8.1 \times 10^4]$ km is approximately estimated by the correlation time $T_c \approx [1{,}300, 2{,}300]$ s and root mean square of the perpendicular fluctuating velocity $\delta V_{p\perp} \approx M_{A,\mathrm{turb}} V_A \approx 35$ km s^{-1}. In Fig. 2, $\hat{I}_A(k_\perp, k_\parallel)$ is normalized as $I_A(k_\perp, k_\parallel)$ by a constant value (one-third of the maximum magnetic energy in all $(k_\perp, k_\parallel)$ bins), as displayed by the colour contours with black dashed curves. The 2D distribution $\hat{D}_{B_A}(k_\perp, k_\parallel)$ shows two different properties: (1) For $k_\perp < 2 \times 10^{-4}$ km^{-1}, $\hat{D}_{B_A}(k_\perp, k_\parallel)$ is mainly concentrated at $k_\parallel < 7 \times 10^{-5}$ km^{-1} and cascading along the $k_\perp$ direction, suggesting that little energy cascades parallel to the background magnetic field, consistent with energy distributions in weak MHD turbulence[6]. (2) For $k_\perp > 2 \times 10^{-4}$ km^{-1}, $\hat{D}_{B_A}(k_\perp, k_\parallel)$ starts to distribute to higher $k_\parallel$, and both wavenumber distributions and intensity changes of $\hat{D}_{B_A}(k_\perp, k_\parallel)$ are almost consistent with $\hat{I}_A(k_\perp, k_\parallel)$. This indicates that $\hat{D}_{B_A}(k_\perp, k_\parallel)$ captures some of the theoretical characteristics of strong MHD turbulence[4]. Besides, $\hat{D}_{B_A}(k_\perp, k_\parallel)$ is in good agreement with the Goldreich–Sridhar scaling $k_\parallel \propto k_\perp^{2/3}$ (ref. 4). This result further confirms that the properties of $\hat{D}_{B_A}(k_\perp, k_\parallel)$ at $k_\perp > 2 \times 10^{-4}$ km^{-1} are closer to those in strong MHD turbulence. The change in $\hat{D}_{B_A}(k_\perp, k_\parallel)$ from purely stretching along the $k_\perp$ direction to following the Goldreich–Sridhar scaling $k_\parallel \propto k_\perp^{2/3}$ reveals a possible transition in the energy cascade.

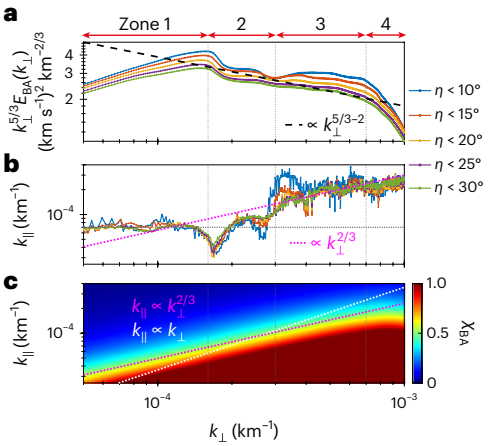

Fig. 3 | Perpendicular wavenumber dependence of the compensated spectra, parallel wavenumber and nonlinearity parameter. **a**, $k_\perp^{5/3} E_{B_A}(k_\perp)$ versus $k_\perp$. The dashed line represents the scaling $k_\perp^{5/3} E_{B_A}(k_\perp) \propto k_\perp^{5/3-2}$. To facilitate comparison with proton velocity fluctuations, magnetic field fluctuations are in Alfvén speed units. **b**, Variation of $k_\parallel$ versus $k_\perp$. The dashed line represents the scaling $k_\parallel \propto k_\perp^{2/3}$. The horizontal dotted line marks $k_\parallel = 7 \times 10^{-5}$ km^{-1}. **c**, $\chi_{B_A}(k_\perp, k_\parallel)$ spectrum calculated using the dataset for $\eta < 30°$. There are four zones: (1) $5 \times 10^{-5} < k_\perp < 1.6 \times 10^{-4}$ km^{-1}, (2) $1.6 \times 10^{-4} < k_\perp < 3 \times 10^{-4}$ km^{-1}, (3) $3 \times 10^{-4} < k_\perp < 7 \times 10^{-4}$ km^{-1} and (4) $7 \times 10^{-4} < k_\perp < 1 \times 10^{-3}$ km^{-1}. The first, second and third vertical dotted lines are around the maximum of $k_\perp^{5/3} E_{B_A}(k_\perp)$, the beginning and the end of flattened $k_\perp^{5/3} E_{B_A}(k_\perp)$, respectively.

Figure 3a shows the compensated spectra ($k_\perp^{5/3} E_{B_A}(k_\perp)$). The magnetic energy spectral density is defined as $E_{B_A}(k_\perp) = \delta B_A^2(k_\perp)/2k_\perp$, where $\delta B_A^2(k_\perp)$ is the magnetic energy density at $k_\perp$ (Methods). In zone 2, $k_\perp^{5/3} E_{B_A}(k_\perp)$ is roughly consistent with $k_\perp^{5/3-2}$ (the dashed line), indicating that the spectral slopes of $E_{B_A}(k_\perp)$ are around −2. In zone 3, on the other hand, $k_\perp^{5/3} E_{B_A}(k_\perp)$ is almost flat, suggesting that $E_{B_A}(k_\perp)$ satisfies the Kolmogorov scaling ($E_{B_A}(k_\perp) \propto k_\perp^{-5/3}$). The sharp change in the spectral slopes of $E_{B_A}(k_\perp)$ from −2 to −5/3 is apparent evidence for the transition of the turbulence regimes[14,15]. In addition, $E_{B_A}(k_\perp) \propto k_\perp^{-1}$ appears in a substantial portion of zone 1, indicating the weak turbulence forcing in action[9,30].

Figure 3b shows the variation of $k_\parallel$ versus $k_\perp$ given the same Alfvénic magnetic energy. In zone 1, as $k_\perp$ increases, $k_\parallel$ is relatively stable at $k_\parallel \approx 7 \times 10^{-5}$ km^{-1}. In zone 3, the variation of $k_\perp$ versus $k_\parallel$ agrees with the

https://doi.org/10.1038/s41550-024-02249-0

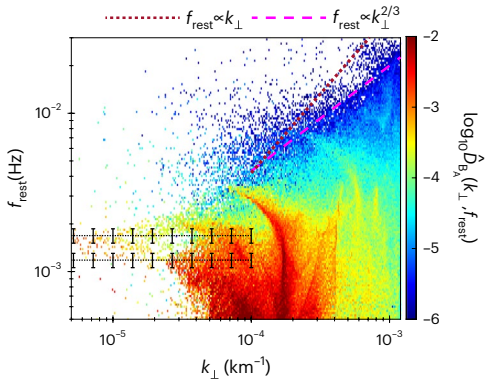

Fig. 4 | The $k_\perp$ versus f_{rest} distributions of Alfvénic magnetic energy in the plasma flow frame. $\hat{D}_{B_A}(k_\perp, f_{rest}) = D_{B_A}(k_\perp, f_{rest})/D_{B_A,max}$ is normalized by the maximum magnetic energy in all ($k_\perp$,f_{rest}) bins. The horizontal dotted lines represent theoretical Alfvén frequencies $f_A = |k_\parallel V_A|/(2\pi)$, where $k_\parallel \approx 7 \times 10^{-5}$ km^{-1} in zone 1 of Fig. 3b, and $k_\parallel \approx 1 \times 10^{-4}$ km^{-1} in zone 1 of Supplementary Fig. 7b. The f_A uncertainties are estimated by the standard deviation of V_A (106 ± 11 km^{-1}), illustrated by error bars on corresponding horizontal dotted lines. This figure utilizes the dataset for $\eta < 30°$.

Goldreich–Sridhar scaling $k_\parallel \propto k_\perp^{2/3}$ (the dashed line). Figure 3c shows $k_\perp$ versus $k_\parallel$ distributions of the nonlinearity parameter $\chi_{B_A}(k_\perp, k_\parallel)$, which is one of the most critical parameters in distinguishing between weak and strong MHD turbulence[5]. Here, $\chi_{B_A}(k_\perp, k_\parallel)$ is calculated from $\frac{k_\perp \delta B_A(k_\perp,k_\parallel)}{k_\parallel B_0}$ (Methods). For the corresponding parallel and perpendicular wavenumbers in Fig. 3b, $\chi_{B_A}(k_\perp, k_\parallel)$ is much less than unity at most wavenumbers in zone 1, whereas in zone 3, $\chi_{B_A}(k_\perp, k_\parallel)$ increases towards unity and follows the scaling $k_\parallel \propto k_\perp^{2/3}$. These results suggest that there is a transition from weak to strong nonlinear interactions, in agreement with theoretical expectations and simulations[5,14,15].

We observe a similar Alfvénic weak-to-strong transition in the measured proton velocity fluctuations (Supplementary Fig. 7). The transition scale (λ_{CB}) is estimated from the smallest perpendicular wavenumber of strong turbulence ($k_{\perp,CB}$), where $\lambda_{CB} \approx 1/k_{\perp,CB}$. For both magnetic field and proton velocity fluctuations, $k_{\perp,CB}$ is around 3×10^{-4} km^{-1}, marked by the second vertical lines in Fig. 3 and Supplementary Fig. 7. The consistency in the transition scales estimated by magnetic field and proton velocity measurements further confirms the reliability of our findings.

A notable perturbation is present in zone 2, as a result of local enhancements of the magnetic energy at $k_\perp \approx 1.8 \times 10^{-4}$ km^{-1} (Fig. 2), leading to the simultaneous existence of strong nonlinearity ($\chi_{B_A} \approx 1$) and weak nonlinearity ($\chi_{B_A} \ll 1$) in the wave number range corresponding to those in Fig. 3b. Thus, the Alfvénic weak-to-strong transition more probably occurs within a 'region' rather than at a critical wavenumber. We do not discuss the fluctuations in zone 4. The deviations in the data for $\eta < 10°$ and $\eta < 15°$ in zone 3 of Fig. 3b are probably due to the limited number of data samples (Supplementary Fig. 6). The uncertainties mentioned above do not affect our main conclusions.

Figure 4 presents f_{rest} versus $k_\perp$ distributions of the magnetic energy, where f_{rest} is the frequency in the plasma flow frame. At $k_\perp < 5 \times 10^{-5}$ km^{-1}, the magnetic energy is concentrated at $f_{rest} \approx f_A$, where f_A is the Alfvén frequency (horizontal dotted lines with error bars). At $k_\perp > 1 \times 10^{-4}$ km^{-1}, the range of f_{rest} broadens, mostly deviating from f_A. Nevertheless, the boundary of fluctuating frequencies is roughly consistent with the scaling $f_{rest} \propto k_\perp^{2/3}$ (the dashed line), indicating that the magnetic energy at these wavenumbers satisfies the scaling $k_\parallel \propto k_\perp^{2/3}$ due to $f_{rest} \propto k_\parallel$ for Alfvén modes. These results suggest that Alfvénic fluctuations with strong nonlinear interactions do not agree with linear dispersion relations but satisfy the wavenumber scaling of Alfvén modes. The change from single-frequency to broadening-frequency fluctuations with increasing $k_\perp$ suggests that there is a possible transition of turbulence regimes.

Table 1 | Transition wavenumbers are determined by magnetic field measurements

	Weak MHD turbulence	Strong MHD turbulence
$k_\parallel$ versus $k_\perp$ distributions of magnetic energy	Purely perpendicular cascade, $k_\perp < 2\times10^{-4}$ km^{-1}	Goldreich–Sridhar cascade, $k_\perp > 2\times10^{-4}$ km^{-1}
Spectral slopes of magnetic energy	Wave-like (−2), $1.6\times10^{-4} < k_\perp < 3\times10^{-4}$ km^{-1}	Kolmogorov-like (−5/3), $3\times10^{-4} < k_\perp < 7\times10^{-4}$ km^{-1}
Nonlinearity parameter (χ_{BA})	$X_{BA} \ll 1$, $k_\perp < 1\times10^{-4}$ km^{-1}	$X_{BA} \approx 1$ and $X_{BA} \geq 1$, $3\times10^{-4} < k_\perp < 7\times10^{-4}$ km^{-1}
Frequency–wavenumber distributions	Single-frequency fluctuations, $f_{rest} \approx f_A$, $k_\perp < 5\times10^{-5}$ km^{-1}	Broadening-frequency fluctuations with $f_{rest} \propto k_\perp^{2/3}$ boundary, $k_\perp > 1\times10^{-4}$ km^{-1}

Discussion

The Alfvénic transition of weak to strong turbulence during cascades to smaller scales is one of the cornerstones of the modern MHD theory. Despite being proposed decades ago, evidence that confirms the existence of the Alfvénic transition is lacking. In this paper, we present direct evidence of the Alfvénic transition at different angles, for example, the transition of energy spectra (Fig. 3a), the Goldreich–Sridhar-type envelope for the nonlinear parameter (Fig. 3c) and the spread of f_{rest} on small scales (Fig. 4; see Table 1 for a summary). Our observation demonstrates that the Alfvénic transition to strong turbulence is bound to occur with an increase of the nonlinearity, even if fluctuations on large scales are considered as 'small amplitude' ($M_{A,turb} \approx 0.33$). Note that the plasma parameters in the analysed event are generic and that the Alfvénic weak-to-strong transition can occur in other astrophysical and space plasma systems. The impact of our findings goes beyond the study of turbulence to particle transport and acceleration[31,32], magnetic reconnection[33,34], star formation[35,36] and all other relevant fields. See, for example, refs. 37,38.

Methods

GSE coordinates

We use the GSE coordinates in this study. X_{GSE} points towards the Sun from the Earth, Z_{GSE} orients along the ecliptic north pole and Y_{GSE} completes a right-handed system.

Trace power spectral densities

The trace power spectral densities of the magnetic field and proton velocities ($P_B = P_{B,X} + P_{B,Y} + P_{B,Z}$ and $P_V = P_{V,X} + P_{V,Y} + P_{V,Z}$) were calculated by applying a fast Fourier transform with three-point centred smoothing in GSE coordinates. We chose the intermediate instant of each time window as the time point at which the spectral slope varies with time.

Alfvén mode decomposition

We calculated the wavenumber–frequency distributions of the Alfvénic magnetic field and proton velocity power with an improved Alfvén mode decomposition method. This method combines the linear decomposition method[8], singular value decomposition (SVD)[23] and a multispacecraft timing analysis[24]. We performed the calculations in each moving time window with a length of 5 h and a moving step of 5 min. The window length selection (5 h) provides low-frequency (large-scale) measurements while ensuring that $\mathbf{B}_0$ approaches the local background magnetic field.

First, we obtained the wavelet coefficients (W) of the magnetic field and proton velocity using Morlet-wavelet transforms[39]. To eliminate the edge effect due to the finite length of the time series, we performed the wavelet transforms for twice the time window length and cutoff of the periods affected.

Second, the wavevector directions ($\mathbf{k}_{SVD}(t,f_{sc})$) were determined by SVD for the magnetic wavelet coefficients[23]. SVD was used to create a real matrix equation ($\mathbf{S}\cdot\hat{\mathbf{k}}_{SVD}=0$) equivalent to the linearized Gauss's law for magnetism ($\mathbf{B}\cdot\hat{\mathbf{k}}_{SVD}=0$). Notice that the minimum singular value of the real matrix $\boldsymbol{S}$ (6 × 3) is the best estimate of wavevector directions but cannot be used to determine the wavenumbers. Since the relative satellite separations were much shorter than the half-wavelength of MHD scales, the properties of the fluctuations simultaneously measured by the four Cluster spacecraft are similar. Thus, the average wavevector direction and background magnetic field are given by $\mathbf{k}_{SVD}=\frac{1}{4}\sum_{i=1,2,3,4}\hat{\mathbf{k}}_{SVD,C_i}$ and $\mathbf{B}_0=\frac{1}{4}\sum_{i=1,2,3,4}\mathbf{B}_{0,C_i}$. C_i denotes the four Cluster spacecraft.

Third, we extracted Alfvénic components from proton velocity fluctuations based on their incompressibility ($\hat{\mathbf{k}}_{SVD}\cdot\delta\mathbf{V}_p=0$) and perpendicular fluctuating directions ($\hat{\mathbf{b}}_0\cdot\delta\mathbf{V}_p=0$) in wavevector space, where $\delta\mathbf{V}_p$ is expressed by vectors of velocity wavelet coefficients, $\hat{\mathbf{k}}_{SVD}=\mathbf{k}_{SVD}/|\mathbf{k}_{SVD}|$, and $\hat{\mathbf{b}}_0=\mathbf{B}_0/|\mathbf{B}_0|$. Similarly, Alfvénic magnetic field fluctuations were extracted from $\hat{\mathbf{k}}_{SVD}\cdot\delta\mathbf{B}=0$ and $\hat{\mathbf{b}}_0\cdot\delta\mathbf{B}=0$, according to the linearized induction equation

$$\omega\delta\mathbf{B}=\mathbf{k}\times(\mathbf{B}_0\times\delta\mathbf{V}_p)\approx|\mathbf{k}|\hat{\mathbf{k}}_{SVD}\times(\mathbf{B}_0\times\delta\mathbf{V}_p),\tag{3}$$

where $\mathbf{k}$ is the wavevector. Thus, Alfvénic proton velocity and magnetic field fluctuations are in the same direction $\hat{\mathbf{k}}_{SVD}\times\hat{\mathbf{b}}_0/|\hat{\mathbf{k}}_{SVD}\times\hat{\mathbf{b}}_0|$ (see the schematic in Supplementary Fig. 4).

Fourth, the Alfvénic magnetic power at each time t and f_{sc} was calculated as $P_{B_A}(t,f_{sc})=\frac{1}{4}\sum_{i=1,2,3,4}W_{B_A,C_i}W^*_{B_A,C_i}$. The Alfvénic proton velocity power was calculated as $P_{V_A}(t,f_{sc})=W_{V_A,C_1}W^*_{V_A,C_1}$. This is because magnetic field data were available from the four Cluster spacecraft, whereas proton plasma data were available only from Cluster-1 during the period analysed.

Fifth, as SVD does not give the magnitude of the wavevectors, we calculated wavevectors ($\mathbf{k}_A(t,f_{sc})$) using the multispacecraft timing analysis based on phase differences between the Alfvénic magnetic field from the four spacecraft[24]. The magnetic field data were interpolated to a uniform time resolution of eight samples per second to give sufficient time resolution. We consider that the wavefront was moving in the direction $\hat{\mathbf{n}}$ with velocity V_w. The wavevector $\mathbf{k}_A=2\pi f_{sc}\mathbf{m}$, where the vector $\mathbf{m}=\hat{\mathbf{n}}/V_w$ and the subscript A represents the Alfvénic component.

$$\begin{pmatrix}\mathbf{r}_2-\mathbf{r}_1\\ \mathbf{r}_3-\mathbf{r}_1\\ \mathbf{r}_4-\mathbf{r}_1\end{pmatrix}\mathbf{m}=\begin{pmatrix}\delta t_2\\ \delta t_3\\ \delta t_4\end{pmatrix},\tag{4}$$

where Cluster-1 has arbitrarily been taken as the reference. The left-hand side of equation (4) contains the relative spacecraft separations. The right-hand side of equation (4) represents the weighted average time delays, estimated by the ratio of six phase differences, $\phi_{ij}=\arctan(\mathcal{S}(W^{ij}_{B_A}),\mathcal{R}(W^{ij}_{B_A}))$, to the angular frequencies, $\omega_{sc}=2\pi f_{sc}$, where ϕ_{ij} is from all spacecraft pairs ($ij=12,13,14,23,24,34$)). $\mathcal{S}$ and $\mathcal{R}$ are the imaginary and real parts of the cross-correlation coefficients, respectively. The four Cluster spacecraft provide six cross-correlation coefficients[39], that is, $W^{12}_{B_A}=\langle W_{B_A,C_1}W^*_{B_A,C_2}\rangle$, $W^{13}_{B_A}=\langle W_{B_A,C_1}W^*_{B_A,C_3}\rangle$, $W^{14}_{B_A}=\langle W_{B_A,C_1}W^*_{B_A,C_4}\rangle$, $W^{23}_{B_A}=\langle W_{B_A,C_2}W^*_{B_A,C_3}\rangle$, $W^{24}_{B_A}=\langle W_{B_A,C_2}W^*_{B_A,C_4}\rangle$ and $W^{34}_{B_A}=\langle W_{B_A,C_3}W^*_{B_A,C_4}\rangle$, where the angular brackets denote a time average over 256 s to ensure the reliability of the phase differences.

Note that a timing analysis was used to determine the actual wavevectors of the Alfvénic magnetic field. In contrast, SVD determines the best estimate of the wavevector sum in three magnetic field components[23]. Thus, $\mathbf{k}_A$ is not completely aligned with $\hat{\mathbf{k}}_{SVD}$. Besides, we restrict our analysis to fluctuations with small angle η between $\hat{\mathbf{k}}_{SVD}$ and $\mathbf{k}_A$ to ensure the reliability of the extraction process (the third step). By relaxing the η constraints, more sampling points are used so that the uncertainty from the limited measurements decreases. On the other hand, with relaxed η constraints, k_A deviates more from k_{SVD}, which may increase the uncertainty. This letter presents results from five datasets for $\eta<10°$, $\eta<15°$, $\eta<20°$, $\eta<25°$ and $\eta<30°$ to investigate the effects of uncertainties introduced by the combination of SVD and a timing analysis.

Sixth, we constructed a set of 400 × 400 × 400 bins to obtain wavenumber–frequency distributions of the magnetic power $P_{B_A}(k_\perp,k_\parallel,f_{sc})$ and proton velocity power $P_{V_A}(k_\perp,k_\parallel,f_{sc})$, where the parallel wavenumber is $k_\parallel=\mathbf{k}_A\cdot\hat{\mathbf{b}}_0$ and the perpendicular wavenumber is $k_\perp=\sqrt{\mathbf{k}_A^2-k_\parallel^2}$. Each bin subtended approximately the same $k_\perp$, $k_\parallel$ and f_{sc}. To cover all MHD wavenumbers and ensure measurement reliability, we restricted our analysis to fluctuations with $1/(100d_{sc})<k<\min(0.1/\max(d_i,r_{cii}),\pi/d_{sc})$ and $2/t^*<f_{rest}<f_{ci}/2$, and fluctuations beyond these wavenumber and frequency ranges were set to zero. Here, d_{sc} is the relative satellite separation, min(*) and max(*) are the minimum and maximum, d_i is the proton inertial length, r_{ci} is the proton gyro-radius, t^* is the duration studied, $f_{rest}=f_{sc}-\mathbf{k}_A\cdot\mathbf{V}_p/(2\pi)$ is the frequency in the plasma flow frame and $\mathbf{V}_p$ is the proton bulk velocity with the spacecraft velocity being negligible. This study utilizes the representation of absolute frequencies:

$$(f_{rest},\mathbf{k}_A)=\begin{cases}(f_{rest},\mathbf{k}_A), & f_{rest}>0,\\ (-f_{rest},-\mathbf{k}_A), & f_{rest}<0.\end{cases}\tag{5}$$

$P_{\epsilon_A}(k_\perp,k_\parallel,f_{sc})$ were obtained by averaging $P_{\epsilon_A}(k_\perp,k_\parallel,f_{sc},t)$ over effective time points in all time windows at each f_{sc} and each $\mathbf{k}$, where $\epsilon=V$ or B represents the proton velocity (V) and magnetic field (B).

Alfvén speed units

For comparison, this study presents the fluctuating magnetic field in Alfvén speed units, which are normalized by $\sqrt{\mu_0 m_p N_0}$, where μ_0 is the vacuum permeability, m_p the proton mass and N_0 the mean proton density.

Magnetic energy spectral density

For this study, we define the energy spectral density of the magnetic field as $E_{B_A}(k_\perp)=\frac{1}{2}\frac{\delta B_A^2(k_\perp)}{k_\perp}$, where the Alfvénic magnetic energy density is calculated as $\delta B_A^2(k_\perp)=2\sum_{k_\perp=k_\perp}^{k_\perp\to\infty}\sum_{k_\parallel=0}^{k_\parallel\to\infty}\int_0^\infty P_{B_A}(k_\perp,k_\parallel,f_{sc})\,\mathrm{d}f_{sc}$.

Nonlinearity parameter

The nonlinearity parameter was estimated with $\chi_{B_A}(k_\perp,k_\parallel)\approx k_\perp\delta B_A(k_\perp,k_\parallel)/(k_\parallel B_0)$, where the Alfvénic magnetic energy density was calculated as $\delta B_A^2(k_\perp,k_\parallel)=\sum_{k_\perp=k_\perp}^{k_\perp\to\infty}\sum_{k_\parallel=k_\parallel}^{k_\parallel\to\infty}\int_0^\infty P_{B_A}(k_\perp,k_\parallel,f_{sc})\,\mathrm{d}f_{sc}$, where B_0 in Alfvén speed units was around 106 km s^{-1}.

Frequency–wavenumber distribution of the magnetic energy

The frequency–wavenumber distributions of the magnetic energy were approximately estimated by $D_{B_A}(k_\perp,f_{sc})\approx\sum_{k_\parallel=0}^{k_\parallel\to\infty}P_{B_A}(k_\perp,k_\parallel,f_{sc})\Delta f_{sc}$ and were transformed into the plasma flow frame by correcting for the Doppler shift $f_{rest}=f_{sc}-\mathbf{k}_A\cdot\mathbf{V}/(2\pi)$.

Data availability

The Cluster data are available at https://cdaweb.gsfc.nasa.gov.

Code availability

Data analysis was performed using the IRFU-MATLAB analysis package available at https://github.com/irfu/irfu-matlab.

References

1. Yan, H. & Lazarian, A. Scattering of cosmic rays by magnetohydrodynamic interstellar turbulence. *Phys. Rev. Lett.* **89**, 281102 (2002).
2. Brunetti, G. & Lazarian, A. Compressible turbulence in galaxy clusters: physics and stochastic particle re-acceleration. *Mon. Not. R. Astron. Soc.* **378**, 245–275 (2007).
3. Bruno, R. & Carbone, V. The solar wind as a turbulence laboratory. *Living Rev. Sol. Phys.* **10**, 2 (2013).
4. Goldreich, P. & Sridhar, S. Toward a theory of interstellar turbulence. 2. Strong Alfvenic turbulence. *Astrophys. J.* **438**, 763 (1995).
5. Howes, G. G., Tenbarge, J. M. & Dorland, W. A weakened cascade model for turbulence in astrophysical plasmas. *Phys. Plasmas* **18**, 102305 (2011).
6. Galtier, S., Nazarenko, S. V., Newell, A. C. & Pouquet, A. Weak turbulence theory for incompressible magnetohydrodynamics. *J. Plasma Phys.* **63**, 447–488 (2000).
7. Mallet, A., Schekochihin, A. A. & Chandran, B. D. Refined critical balance in strong Alfvénic turbulence. *Mon. Not. R. Astron. Soc. Lett.* **449**, L77–L81 (2015).
8. Cho, J. & Lazarian, A. Compressible magnetohydrodynamic turbulence: mode coupling, scaling relations, anisotropy, viscosity-damped regime and astrophysical implications. *Mon. Not. R. Astron. Soc.* **345**, 325–339 (2003).
9. Makwana, K. D. & Yan, H. Properties of magnetohydrodynamic modes in compressively driven plasma turbulence. *Phys. Rev. X* **10**, 031021 (2020).
10. Zhu, X. et al. Wave composition, propagation, and polarization of magnetohydrodynamic turbulence within 0.3 au as observed by Parker Solar Probe. *Astrophys. J.* **901**, L3 (2020).
11. Chaston, C. C. et al. MHD mode composition in the inner heliosphere from the Parker Solar Probe's first perihelion. *Astrophys. J. Suppl. Ser.* **246**, 71 (2020).
12. Zhao, S. Q. et al. Analysis of magnetohydrodynamic perturbations in the radial-field solar wind from Parker Solar Probe observations. *Astrophys. J.* **923**, 253 (2021).
13. Zhao, S. Q. et al. Multispacecraft analysis of the properties of magnetohydrodynamic fluctuations in sub-Alfvénic solar wind turbulence at 1 au. *Astrophys. J.* **937**, 102 (2022).
14. Verdini, A. & Grappin, R. Transition from weak to strong cascade in MHD turbulence. *Phys. Rev. Lett.* **109**, 025004(2012).
15. Meyrand, R., Galtier, S. & Kiyani, K. H. Direct evidence of the transition from weak to strong magnetohydrodynamic turbulence. *Phys. Rev. Lett.* **116**, 105002 (2016).
16. Escoubet, C. P., Fehringer, M. & Goldstein, M. The Cluster mission. *Ann. Geophys.* **19**, 1197–1200 (2001).
17. Balogh, A. et al. The Cluster magnetic field investigation. *Space Sci. Rev.* **79**, 65–91 (1997).
18. Rème, H. et al. First multispacecraft ion measurements in and near the Earth's magnetosphere with the identical Cluster ion spectrometry (CIS) experiment. *Ann. Geophys.* **19**, 1303 (2001).
19. Décréau, P. M. et al. Whisper, a resonance sounder and wave analyser: performances and perspectives for the Cluster mission. *Space Sci. Rev.* **79**, 157–193 (1997).
20. Hadid, L. Z. et al. Nature of the MHD and kinetic scale turbulence in the magnetosheath of Saturn: Cassini observations. *Astrophys. J. Lett.* **813**, L29 (2015).
21. Hadid, L. Z. et al. Compressible magnetohydrodynamic turbulence in the Earth's magnetosheath: estimation of the energy cascade rate using in situ spacecraft data. *Phys. Rev. Lett.* **120**, 55102 (2018).
22. Sahraoui, F., Hadid, L. & Huang, S. Magnetohydrodynamic and kinetic scale turbulence in the near-Earth space plasmas: a (short) biased review. *Rev. Mod. Phys.* **4**, 4 (2020).
23. Santolík, O., Parrot, M. & Lefeuvre, F. Singular value decomposition methods for wave propagation analysis. *Radio Sci.* **38**, 1010 (2003).
24. Pincon, J. L. & Glassmeier, K. H. in *Multi-Spacecraft Analysis Methods Revisited* (eds. Paschmann, G. & Daly, P. W.) 47–54 (ISSI, 2008) .
25. Galtier, S., Nazarenko, S. V., Newell, A. C. & Pouquet, A. Weak turbulence of anisotropic shear-Alfvén waves. *AIP Conf. Proc.* **679**, 518–521 (2003).
26. Nazarenko, S. 2D enslaving of MHD turbulence. *New J. Phys.* **9**, 307–307 (2007).
27. Cho, J. & Vishniac, E. T. The anisotropy of magnetohydrodynamic Alfvenic turbulence. *Astrophys. J.* **539**, 273–282 (2000).
28. He, J.-S. et al. Two-dimensional correlation functions for density and magnetic field fluctuations in magnetosheath turbulence measured by the Cluster spacecraft. *J. Geophys. Res.* **116**, A06207 (2011).
29. Yan, H. & Lazarian, A. Cosmic ray propagation: nonlinear diffusion parallel and perpendicular to mean magnetic field. *Astrophys. J.* **673**, 942–953 (2008).
30. Schekochihin, A. A., Nazarenko, S. V. & Yousef, T. A. Weak Alfvén-wave turbulence revisited. *Phys. Rev. E* **85**, 036406 (2012).
31. Schlickeiser, R. *Cosmic Ray Astrophysics* (Springer, 2002).
32. Yan, H. Magnetohydrodynamic turbulence and propagation of cosmic rays: theory confronted with observations. In *37th International Cosmic Ray Conference* https://doi.org/10.22323/1.395.0038 (2022).
33. Matthaeus, W. H. & Lamkin, S. L. Turbulent magnetic reconnection. *Phys. Fluids* **29**, 2513–2534 (1986).
34. Lazarian, A. & Vishniac, E. T. Reconnection in a weakly stochastic field. *Astrophys. J.* **517**, 700–718 (1999).
35. Crutcher, R. M. Magnetic fields in molecular clouds. *Annu. Rev. Astron. Astrophys.* **50**, 29–63 (2012).
36. Padoan, P. et al. in *Protostars and Planets VI* (eds Beuther, H. et al.) 77–100 (Univ. of Arizona Press, 2014).
37. Zhang, B. & Yan, H. The internal-collision-induced magnetic reconnection and turbulence (ICMART) model of gamma-ray bursts. *Astrophys. J.* **726**, 90 (2011).
38. Hirashita, H. & Yan, H. Shattering and coagulation of dust grains in interstellar turbulence. *Mon. Not. R. Astron. Soc.* **394**, 1061–1074 (2009).
39. Grinsted, A., Moore, J. C. & Jevrejeva, S. Application of the cross wavelet transform and wavelet coherence to geophysical time series. *Nonlinear Proc. Geophys.* **11**, 561–566 (2004).

Acknowledgements

We would like to thank the members of the Cluster spacecraft team and NASA's Coordinated Data Analysis Web. K.H.Y. is supported by the Laboratory Directed Research and Development programme of Los Alamos National Laboratory (Grant No. 20220700PRD1).

Author contributions

H.Y. initiated and designed the project. S.Z. and T.Z.L. designed and completed the data processing methods. S.Z. carried out the specific observation data processing. S.Z., H.Y., T.Z.L., K.H.Y. and H.W. contributed to the theoretical analysis of the main results. All authors contributed to writing, editing and approving the manuscript.

Funding

Open access funding provided by Deutsches Elektronen-Synchrotron (DESY).

Competing interests

The authors declare no competing interests.

Additional information

Supplementary information The online version contains supplementary material available at https://doi.org/10.1038/s41550-024-02249-0.

Correspondence and requests for materials should be addressed to Huirong Yan or Terry Z. Liu.

Peer review information *Nature Astronomy* thanks the anonymous reviewers for their contribution to the peer review of this work.